nature communications

Article

https://doi.org/10.1038/s41467-024-51940-3

Spatially structured exchange of metabolites enhances bacterial survival and resilience in biofilms

Received: 7 May 2024

Accepted: 21 August 2024

Published online: 31 August 2024

Check for updates

Yuzhen Zhang[1,3,4] ✉, Yukmi Cai[1,3], Bing Zhang[2] & Yi-Heng P. Job Zhang[1,4] ✉

Biofilm formation enhances bacterial survival and antibiotic tolerance, but the underlying mechanisms are incompletely understood. Here, we show that biofilm growth is accompanied by a reduction in bacterial energy metabolism and membrane potential, together with metabolic exchanges between the inner and outer regions in biofilms. More specifically, nutrient-starved cells in the interior supply amino acids to cells in the periphery, while peripheral cells experience a decrease in membrane potential and provide fatty acids to interior cells. Fatty acids facilitate the repair of starvation-induced membrane damage in inner cells and enhance their survival in the presence of antibiotics. Thus, metabolic exchanges between inner and outer cells contribute to survival of the nutrient-starved inner cells and contribute to antibiotic tolerance within the biofilm.

Biofilms, the predominant mode of microbial life[1–3], are considered a successful evolutionary adaptation for bacteria. They possess enhanced survival and tolerance abilities, enabling them to better adapt to environmental fluctuations[4,5], withstand antibiotic treatments[2,6–11], and evade host clearance[12,13], thus achieving remarkable success in survival.

However, the question remains: How do biofilms acquire these traits? Several studies have reported the physical protection provided by the extracellular matrix[10,14,15], while an increasing amount of evidence suggests that physical barriers are not a primary factor[16–18]. Metabolite exchange has emerged as a crucial aspect of microbial physiology within community structures, which has been shown to facilitate cross-feeding and collective survival[14,19–26]. For instance, cells that acquire lysine from the environment exhibit enhanced protection against oxidants[22]. Spatially structured alanine cross-feeding in biofilms influenced cellular viability and growth[26]. A spatiotemporal cross-feeding mechanism was discovered to fuel *Bacillus subtilis* swarm development: during their migration, earlier generations deposit metabolites which are consumed by later generations that swarm across the same location[27]. Wang et al. revealed that cross-regional resource allocation, local cycling, and feedback signaling in *Escherichia coli* (*E. coli*) biofilms create a nutrient-limited region within the community, sustaining a surprisingly high level of metabolism with potential social functions[25]. Hence, this intricate interplay of metabolic interactions within microbial communities highlights the adaptability and resilience of these systems. However, the roles of metabolite exchange and spatial coordination in enhancing community survival and tolerance during the transition of bacterial individuals into communities remain inadequately analyzed.

Here, employing designed quantitative microfluidics and spatial multi-omics techniques for biofilms, we investigate the temporal and spatial physiological changes from individual bacteria to a biofilm. By uncovering the differences between individual cells and communities, we elucidate the mechanisms underlying the enhanced survival and tolerance abilities in biofilms.

[1]Key Laboratory of Engineering Biology for Low-Carbon Manufacturing, In Vitro Synthetic Biology Center, Tianjin Institute of Industrial Biotechnology, Chinese Academy of Sciences, Tianjin, China. [2]School of Information Science and Engineering, Yanshan University, Qinhuangdao, China. [3]These authors contributed equally: Yuzhen Zhang, Yukmi Cai. [4]These authors jointly supervised this work: Yuzhen Zhang, Yi-Heng P. Job Zhang. ✉e-mail: zhangyzh@tib.cas.cn; zhang_xw@tib.cas.cn

Results

Membrane potential and energy metabolism decrease as biofilm size increases, leading to increase in antibiotic tolerance

To investigate the physiological changes that occur during the development of biofilms from individual bacteria to communities, we developed a quantitative microfluidic technique to study *E. coli* biofilms[28] (Fig. 1a). In our microfluidic system, a fluid flows at a constant rate from the inlet to the outlet (orange arrow in Fig. 1a). The chamber dimensions are in millimeters for length and width while the height remains at a small 6 µm. This leads to the formation of a pancake-like biofilm filling the entire height, resulting in a uniform density along its length and width. The biofilm can only expand in the two-dimensional plane (red arrow in Fig. 1a). Using time-lapse microscopy, we can successfully quantify the spatiotemporal dynamics of the biofilm development process. The fluid is unable to pass through the upper and lower surfaces of the biofilm; it can only flow around the periphery. Nutrients enter the biofilm through diffusion from the periphery, creating a unidirectional flow from the periphery toward the interior of the biofilm.

In the M63B1 medium[29] with glucose as the sole carbon source, there is significant differentiation within the biofilm once it reached a certain size. The periphery of the biofilm has sufficient

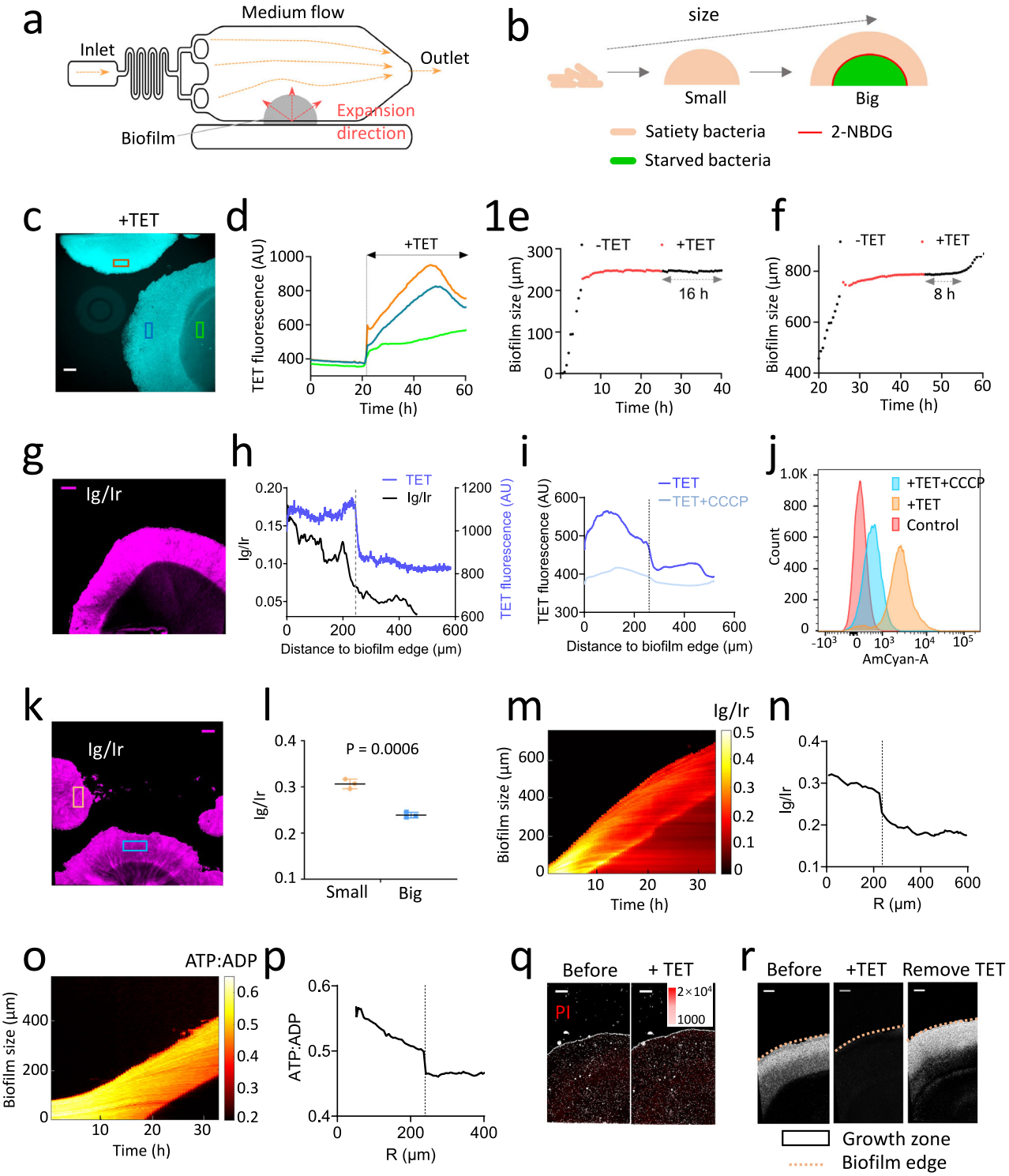

Fig. 1 | Membrane potential and energy metabolism decrease while antibiotic tolerance increase as biofilm community size increases. a Top view of the microfluidic device used to culture bacterial biofilms in this study. The dimensions of growth chamber are Length × Width × Height = 9 mm × 2.4 mm × 6 μm. The orange arrow indicates the direction of medium flow. The gray semicircle illustrates a biofilm formed in the growth chamber. The red arrow indicates the direction of biofilm expansion. **b** Schematic of biofilm development from single cells to larger communities. The red line indicates the position of 2-NBDG, delineating the periphery glucose-rich zone and the interior glucose-starved zone. **c** Snapshot of tetracycline (TET, 5 μg/ml) fluorescence after 20 h of treatment in the biofilms. Scale bar, 100 μm. **d** Dynamics of TET fluorescence in biofilms as shown in (**c**). Growth of biofilms before, during, and after 25 μg/ml TET treatment. TET was added when the biofilm size was 220 μm (**e**) and 700 μm (**f**), respectively. **g** Membrane potential distribution in *E. coli* biofims, as indicated by the fluorescent sensor ViBac2. Ig/Ir means the ratio of Arclight fluorescence intensity (Ig) to that of mCherry-L (Ir), utilized as an indicator of the relative membrane potential. Scale bar, 100 μm. Representative of >3 biological replicates. **h** Distribution pattern of membrane potential was highly consistent with that of TET. The TET was added for 24 h. The black line denotes the membrane potential (Ig/Ir) profile, and the bluish violet line represents the TET profile. **i** The spatial distribution of TET under 20 μM CCCP added or not. The TET was added for 24 h. **j** TET (2 μg/ml) accumulation rate in planktonic bacteria under 20 μM CCCP added or not, as determined by flow cytometry. The control group with no TET and no CCCP added. **k** Membrane potential (Ig/Ir) distribution in *E. coli* biofims, as indicated by the fluorescent sensor ViBac2. Scale bar, 100 μm. **l** Membrane potential (Ig/Ir) in biofilms as shown in (**k**). Data are presented as mean values ± SD, 3 biological replicates. Statistical significance was determined by two-sided Student's *t*-tests: *P* value = 0.0006. **m** Kymograph of membrane potential in an *E. coli* biofilm as it develops from a small to big size under 1× glucose conditions. **n** Dynamics of membrane potential as biofilm size increases. The membrane potential (Ig/Ir) was calculated as the average value at the biofilm's peripheral 50 μm. **o** Kymograph of ATP:ADP distribution in *E. coli* biofilm as it develops from a small to big size. **p** Dynamics of ATP:ADP ratios as biofilm size increases. The ATP:ADP values were averaged at the biofilm's peripheral 50 μm. **q** Cell death (propidium iodide (PI) signal) in the biofilm before and after 25 μg/ml tetracycline treatment for 20 h. Images are composites of phase contrast and fluorescence. Red represents PI fluorescence. All snapshots are displayed with the same contrast settings. The images are representative of at least 3 biological replicates. Scale bars, 100 μm. **r** Growth zone, revealed by image differencing (imDiff) ("Methods" section) in the biofilm before, during and after antibiotic treatment. Scale bar, 100 μm. Representative of >3 biological replicates. Source data are provided as a Source Data file.

glucose for growth, while cells in the interior experience glucose starvation and are unable to grow[28] (Fig. 1b; Supplementary Fig. 1). This is due to the fact that nutrients diffuse unidirectionally from the periphery to the interior. After reaching a certain depth within the biofilm, glucose is completely depleted. Here, we used a fluorescent glucose analog 2-(*N*-(7-nitrobenz-2-oxa-1,3-diazol-4-yl) amino)-2-deoxyglucose (2-NBDG)[30,31] to conveniently characterize glucose gradient in the biofilm. We found 2-NBDG accumulated in a ring at a depth of 230 μm from the edge of biofilm under 1× glucose (22 mM) (Supplementary Fig. 2a). It's known that uptake rate of 2-NBDG by *E.coli* is highly dependent on glucose concentration[30]. Under glucose-rich conditions, bacteria preferentially uptake glucose, and if the glucose concentration decreases to <10 μM, then bacteria accelerate the uptake of 2-NBDG[30] (Supplementary Fig. 2b). After entering the cell, 2-NBDG can be degraded into a non-fluorescent form in ~30 min[30,31]. Together, the increased uptake rate as well as 2-NBDG's degradation resulted in the visualization of a ring pattern within the biofilms. Indeed, we observe that 2-NBDG fluorescence is abruptly enhanced in individual bacteria after switching the medium without glucose (Supplementary Fig. 2c). Moreover, by using a fluorescent reporter strain P*ptsG-yfp* (Supplementary Fig. 2d), which promoter is activated by glucose limitation[32], we found a high degree of overlap between the locations where P*ptsG* is activated and the locations of 2-NBDG in the biofilm (Supplementary Fig. 2e). These results indicated that 2-NBDG fluorescence is a good indicator of the location of glucose depletion in biofilms (Supplementary Fig. 2f). Based on these observations, we noted the emergence of an interior glucose-starved zone in biofilms when their size surpassed 230 μm under 1× glucose (Supplementary Fig. 3). In this work, we defined biofilms without a glucose-starved zone (without 2-NBDG band) as small biofilms, and those with an interior glucose starvation zone (with 2-NBDG band) as big biofilms or mature biofilms.

Tetracycline, a fluorescent antibiotic, exhibits fluorescence intensity corresponding to its intracellular concentration[33]. We observed that tetracycline mainly distributes at the periphery of big biofilms or fully in the small biofilm[33] (Fig. 1c). Notably, the rate of tetracycline accumulation in small biofilms was significantly higher compared to big biofilms (Fig. 1d). The intracellular accumulation of antibiotics is necessary for their pharmacological effectiveness. Consequently, small biofilms exhibit significantly longer recovery time for growth compared to big biofilms under the same treatment conditions. When a small biofilm with a size of 220 μm was treated with tetracycline for 20 h (after which the drug was removed), the biofilm failed to resume growth within 16 h (Fig. 1e). In contrast, the big biofilm of a size of 720 μm resumed growth in <8 h under the same treatment conditions (Fig. 1f). Similar effects were observed when the antibiotics kanamycin, ciprofloxacin, and ceftazidime were used (Supplementary Fig. 4). These results demonstrate that as the size of the biofilms increases, their tolerance to tetracycline, as measured by the ability to resume growth, becomes stronger.

Tetracycline accumulation in susceptible *E.coli* is energy dependent and driven by membrane potential[33–37]. Here, by employing ViBac2[38], which is a genetically encoded sensor that exhibit significant fluorescent intensity changes in response to membrane voltage changes, we showed that the membrane potential of peripheral bacteria in biofilm is higher than that in interior bacteria (Fig. 1g) and the membrane potential abruptly transition at the same point where glucose becomes depleted (Supplementary Fig. 5a). Moreover, we found that the tetracycline accumulation pattern is coincided with the spatial distribution of membrane potential (Fig. 1h). When adding 20 μM carbonyl cyanide m-chlorophenylhydrazone (CCCP), an uncoupler of the proton gradient established during oxidative phosphorylation, which did not influence the biofilm growth (Supplementary Fig. 5b), membrane potential was reduced (Supplementary Fig. 5c) and biofilm periphery accumulated less tetracycline (Fig. 1i; Supplementary Fig. 5d, e). This result was also validated in the planktonic bacteria (Fig. 1j). These findings demonstrated that tetracycline enrichment in the biofilm is determined by its membrane potential.

Based on these findings, we hypothesized that membrane potentials between big and small biofilms should be different. Indeed, we discovered that the membrane potential of small biofilms was ~40% higher than that of big biofilms (Fig. 1k, l). In our previous work, we also observed that the membrane potential of planktonic bacteria was 65% higher than that of big biofilms[33]. These outcomes indicate that as the community expands, the membrane potential declines. To investigate this further, we compared the membrane potential of *E. coli* biofilms during their development from small to big. Interestingly, we observed a sharp decrease in membrane potential (Fig. 1m, n) when the biofilm size exceeded 230 μm, which corresponded with the emergence of an interior glucose starvation region (Supplementary Fig. 5a). Additionally, we used PercevalHR[39] a genetically encoded sensor that senses the bacterial ATP:ADP ratio by calculating the ratio metric value (F500/F420), to visualize the ATP:ADP distribution. We found ATP:ADP distribution exhibited a significant decline once the biofilm size surpassed 230 μm (Fig. 1o, p), again coinciding with the presence of interior

glucose-starved bacteria (Supplementary Fig. 5f). Both of the two sensors indicated that as the biofilm size increases, its energy metabolism and membrane potential sharply decline coinciding with the emergence of interior glucose-starved bacteria, which could cause the decrease in the antibiotic accumulation in biofilms and increase their tolerance to antibiotic.

By comparing the fluorescence intensity of propidium iodide (PI), a membrane impermeant dye that is generally excluded from viable cells[40], before and after 25 μg/ml tetracycline treatment, we discovered that PI intensity was not obviously enhanced by tetracycline treatment for 20 h (Fig. 1q; Supplementary Fig. 6). Furthermore, we measured the growth zones (revealed by image differencing (imDiff), "Methods" section) of the biofilm before and after tetracycline treatment. We found that after tetracycline withdrawal, the biofilm growth zone remained at the periphery, as shown in Fig. 1r. These results suggest that the treatment of tetracycline under such concentration did not cause obviously mortality among peripheral bacteria. Hence, the differences in antibiotic accumulation rates and antibiotic tolerance in biofilms with different sizes are not caused by differences in size. Instead, they are caused by differences in physiological characteristics, such as membrane potential.

Secretion of amino acids by interior-starved bacteria triggers a decrease in peripheral membrane potential to enhance antibiotic tolerance

Due to the constant supply of fresh M63B1 medium in the microfluidic chamber, glucose was always abundant to the peripheral bacteria in biofilm[33]. This was demonstrated by the constant width of the 2-NBDG band during biofilm expansion (Supplementary Fig. 3c). This indicates that the decrease in energy metabolism and membrane potential during biofilm development is not due to a lack of nutrients but a spontaneous collective behavior, resulting from biofilm adaptation.

Given this, we turned to answer why the membrane potential and energy metabolism spontaneously decrease with the biofilm size increase. Using both ATP:ADP sensor and membrane potential sensor, we demonstrated that as the biofilm size increased and surpassed 230 μm (Fig.1n, p), energy metabolism and membrane potential of peripheral bacteria sharply declined, coinciding with the emergence of interior glucose-starved bacteria. Therefore, there were potentially two factors impacting this collective behavior: biofilm size and the interior-starved bacteria. Similar to quorum sensing[41,42], if this collective behavior depended on biofilm size or density, then membrane potential would decrease once the biofilm exceeded certain size (230 μm, Fig.1n, p), regardless of glucose concentration. To test this, we reduced glucose concentration in the medium (Fig. 2a–c), and observed a decrease in membrane potential of peripheral bacteria even at smaller biofilm sizes. Due to the reduced glucose concentration, the glucose penetration depth would be narrower[28] (Supplementary Fig. 2f) and interior-starved bacteria appear at smaller sizes. Our findings demonstrated that the membrane potential decrease corresponded to the appearance of interior-starved bacteria, rather than being restricted to a specific size (Fig.2a–c; Supplementary Fig. 7), suggesting that the emergence of interior-starved bacteria caused a decrease in peripheral membrane potential.

To investigate how interior-starved bacteria regulate the decrease in peripheral membrane potential, we developed a spatial multi-omics method applicable to the biofilm (Fig. 2d; "Methods" section). Utilizing the 2-NBDG band, we divided the mature biofilm into two regions: an interior glucose-deficient region and a peripheral glucose-abundant region. We then subjected each part to multi-omics analysis. A small biofilm only has the peripheral region available for analysis.

To understand the physiological differences during biofilm development, we conducted proteomics and ^{13}C-labeled metabolomics analysis, comparing the periphery of a big biofilms with small biofilms (Fig. 2e–g). The small biofilms lack an interior region depleted of glucose, and both the periphery of big biofilms and the entire small biofilms are in a glucose-sufficient environment and capable of growth (Supplementary Fig. 1), making them comparable. By applying data-independent acquisition (DIA) mass spectrometry, bacteria protein expression level was quantified by peptide abundances that calculated from the peak value in MS/MS profile ("Methods" section). Based on the fold change values of protein abundance between peripheral bacteria in big biofilm and in small biofilm, we observed that as the biofilm size increased, amino acids synthesis pathway was significantly downregulated in the peripheral bacteria (Fig. 2e; Supplementary Fig. 8). Specifically, apart from a slight increase in the protein abundance of serine and threonine synthesis, the protein abundance of other amino acids synthesis in big biofilm peripheral bacteria showed a decrease (Fig. 2f). Additionally, by switching from glucose ^{12}C to glucose (U6-^{13}C) in the medium and labeling for 10 h, the relative ^{13}C-labeled amino acids proportion in peripheral bacteria of big biofilm was lower than that in small biofilm (Fig. 2g), suggesting a decline in the ability for de novo synthesis of amino acids with the growth of biofilm.

Amino acids synthesis relies heavily on glycolysis and the TCA cycle pathways, which are also the main production sources of NADH[43], the primary driving force for the electron respiratory chain[44]. Thus, we hypothesized that the decrease in de novo synthesis of amino acids in peripheral bacteria could be the underlying cause for the reduction in membrane potential and energy metabolism. Consistent with this, transcriptome analysis demonstrated a downregulation in the instantaneous activities of the TCA cycle and oxidative phosphorylation (Supplementary Fig. 9).

However, it remained unclear why peripheral amino acid synthesis decreased despite the unchanged nutrient supply, as well as the specific relationship between this phenomenon and interior-starved bacteria. To gain further insights, we compared the intracellular and extracellular metabolomics of the interior and periphery regions of the big biofilm (Fig. 2h, i). Intracellular metabolomics revealed that the content of free amino acids in the biofilm interior was significantly higher than that in the periphery (Fig. 2h; Supplementary Fig. 10a, b). Similarly, extracellular metabolomics indicated that free amino acids in the interior matrix were notably more abundant than in the peripheral matrix (Fig. 2i; Supplementary Fig. 10c, d). These findings suggest that the amino acids present in the biofilm interior have the potential and may be supplied to the periphery. According to existing literature[45], when the metabolites are present in the extracellular environment at sufficient concentrations, they inhibit their own biosynthetic pathways and instead take up the available metabolites produced by co-growing cells. Indeed, by switching the sole carbon source from glucose ^{12}C to glucose (U6-^{13}C) in the medium, we found that the central carbon metabolites pool was labeling nearly at a 100% ^{13}C/^{12}C ratio in the newly growing bacteria at the periphery after labeled for 10 h (Supplementary Fig. 11). However, the amino acids metabolites pool ^{13}C-labeled proportion was relatively low, only 40%–80% (Supplementary Fig. 11). This result suggests that amino acids may not be entirely synthesized de novo but rather partially obtained from the interior supply. Hence, these results indicate that amino acids secreted by interior-starved bacteria could supply to the periphery (Fig. 3a), reducing the need for de novo synthesis and and subsequently decreasing the energy metabolism and membrane potential in the peripheral region.

To validate this hypothesis, we examined the expression of amino acid importers at the biofilm periphery. The data revealed that as the size of the biofilm increased, the expression levels of various amino acid importers also increased (Fig. 3b). This suggests that the transport of amino acids from extracellular was enhanced. Building on this finding, we made a prediction that if exogenous amino acids were added to a small biofilm to simulate the amino acids secretion by interior-starved bacteria, the membrane potential of the small biofilm

https://doi.org/10.1038/s41467-024-51940-3

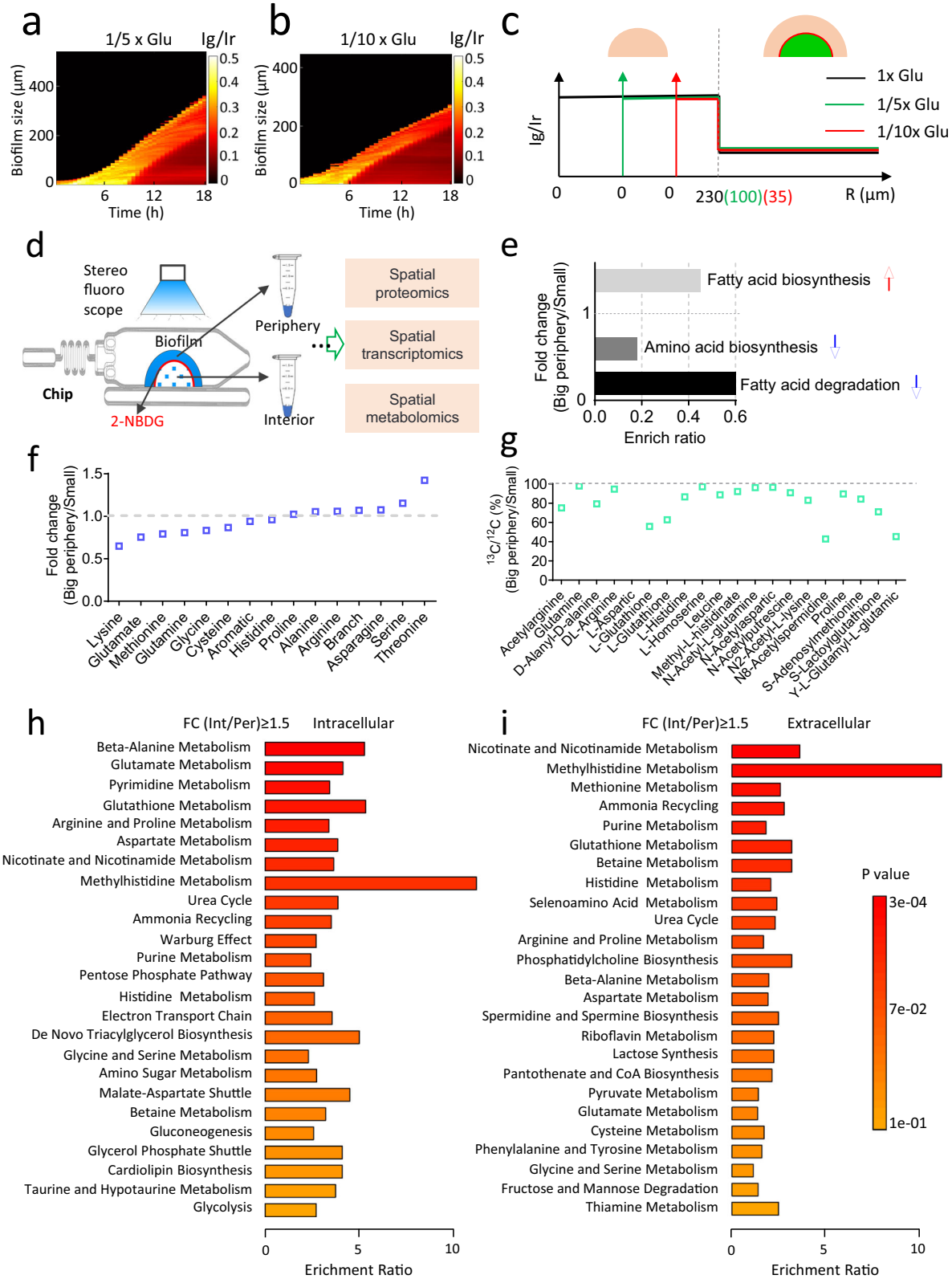

Fig. 2 | Spatial multi-omics reveals that the synthesis of peripheral amino acids decrease and the secretion of interior amino acids increase as biofilm size increase. a, **b** Kymographs of membrane potential in *E. coli* biofilm as it develops from small to big size under 1/5× glucose and 1/10× glucose conditions, respectively. **c** Schematic illustrating the decrease in membrane potential in biofilms under different glucose concentrations. **d** Workflow showing the spatial multi-omics analysis of the biofilm. The dimension of this chamber is Length × Width × Height = 12 mm × 4 mm × 100 μm. Under stereofluoscope, we divided a mature biofilm along the 2-NBDG band into two regions: an interior glucose-deficient region and a peripheral glucose-abundant region. The protein mass of each part could reach 10 μg, which meets the requirements for proteomic analysis. **e** Overview of proteomic changes with increasing biofilm size. **f** Expression of amino acid synthesis proteins as biofilm size increases. For a certain amino acid with multiple synthesis proteins, the average value was taken. **g** $^{13}C/^{12}C$ ratio in intracellular amino acids in biofilms after glucose (^{12}C) is replaced with glucose ($U\text{-}^{13}C_6$) for 4 h. **h** Enrichment analysis of intracellular metabolites. **i** Enrichment analysis of extracellular metabolites. Statistical significance was determined by two-sided Student's *t*-tests in (**h**, **i**). Source data are provided as a Source Data file.

would decrease prematurely. Indeed, our observations confirmed this prediction. When artificially pre-mixed amino acids were added to the medium, the membrane potential of the small biofilm decreased compared to the control group (Fig. 3c–e). Moreover, the addition of pre-mixed amino acids led to a decrease in tetracycline accumulation in small biofilm (Fig. 3f–h) and shortened the recovery time after the drug withdrawal (Fig. 3i–k). These collective findings indicate that as the biofilm develops, emergent interior-starved bacteria resulting from nutrient gradients, provide amino acids to the periphery. This, in turn, induces metabolic reprogramming and reduces the membrane potential of peripheral bacteria, thereby enhancing collective antibiotic tolerance.

Increased levels of fatty acids in the periphery, induced by interior amino acids secretion, diffuse back to the interior to improve survival of starved bacteria

Why the nutrient-poor bacteria of the interior assisted the nutrient-rich bacteria by means of amino acid secretion was still uncertain. We overlooked peripheral fatty acid (FA) synthesis in Fig. 2e, while it is worth noting that the expression of enzymes involved in the FA synthesis pathway increased as the biofilm size expanded. Figure 3l demonstrated that the expression of proteins involved in FA synthesis at the periphery were significantly upregulated with increasing biofilm size. It is important to note that most amino acid synthesis pathways share a common precursor, Acetyl-CoA, with the FA synthesis pathways. Thus, we speculate that the interior-starved bacteria provide amino acids to the periphery, leading to a decrease in de novo amino acid synthesis and subsequently promoting peripheral FA synthesis.

To validate this hypothesis, we introduced artificially pre-mixed amino acids to the medium to simulate the amino acids secretion by interior bacteria. Lipidome analysis revealed a quantitative increase in total lipid content of small biofilm under addition of exogenous amino acids (Fig. 3m; Supplementary Fig. 12). This suggests that the biofilm takes up external amino acids, thereby reducing the need for de novo amino acid synthesis while promoting FA synthesis.

According to our proteomic analysis, the expression of key enzymes responsible for lipid β-oxidation in the biofilm interior increased significantly compared to the periphery (Figs. 2e and 4a). The increase in biofilm size leads to an enhancement of FA synthesis in the biofilm periphery and an enhancement of β-oxidation in the interior. This observation has led us to speculate that the increased FA is intended to supply the interior.

To validate our speculation, we investigated the potential phenotypes resulting from the loss of genes involved in FA transport and synthesis. FadD plays a crucial role in the transport of exogenous FAs prior to their subsequent degradation or incorporation into phospholipids[46]. Loss of the *fadD* gene leads to decreased import of exogenous long-chain FAs[46,47]. FabH, on the other hand, is responsible for the initial step in FAs elongation, and its knockout significantly reduces FA synthesis[48–50]. We observed that the fluorescence intensity of dichloro-dihydro-fluorescein diacetate (DCFH-DA) in the interior of both Δ*fadD* and Δ*fabH* biofilms was brighter compared to the wild type (WT) biofilm (Fig. 4b–d). DCFH-DA is a kind of reactive oxygen species (ROS) dye[51]. Its increased fluorescence indicates that deficiency in FA synthesis (Δ*fabH*) of degradation (Δ*fadD*) lead to increased ROS production in the biofilm interior (Fig. 4b, c). The knockout of *fabH* did not affect ROS accumulation in the periphery, while having a significantly impact on the biofilm interior. These findings suggest a higher demand for FAs in the biofilm interior and imply that the demanded FAs primarily come from the peripheral supply.

Supporting this notion, we compared the lipidome in the extracellular matrix between the Δ*fabH* and WT biofilms. Results showed that the lipid content in the peripheral matrix of the Δ*fabH* biofilm was lower than that in the WT (Fig. 4e; Supplementary Fig. 13a), suggesting an insufficient supply of FAs to the interior. Indeed, when FAs were initially supplemented in the culture medium during Δ*fabH* biofilm cultivation, no obvious ROS production was observed in the biofilm interior (Fig. 4f), similar to the results seen in the WT biofilm. These findings indicate that glucose-starved bacteria in the biofilm interior have a high demand for FAs, and their main source of FAs are coming from peripheral bacteria.

Next, we investigated why the interior bacteria require FAs and what they are used for. First, we can rule out the possibility of FAs being used as a carbon source for bacterial growth (Supplementary Fig. 13b). It is well-established in the literature[52] that the increase in ROS level can be attributed to an increase in the NAD^+:NADH ratio. In this study, we observed a similar effect of ROS production in Δ*fabH* biofilms due to a deficiency in FA supply (Fig. 4c). Thus, we hypothesized that the rise of ROS level was caused by the increase of intracellular NAD^+:NADH ratio under glucose starvation in the biofilm interior. To test this, we used a SoNar[53] sensor to detect the distribution of NAD^+:NADH in the biofilms. SoNar (sensor of NADH redox) is a genetically encoded sensor that can track NAD^+:NADH ratio changes by inducing sensor fluorescent excitation spectrum changes (420 nm when binding NAD^+, 500 nm when binding NADH)[53]. We found that the NADH:NAD^+ ratio in the biofilm interior was relatively low (Fig. 4g), and when the glucose in the media was removed, the NADH:NAD^+ ratio in the periphery would also sharply decrease (Fig. 4h). These results suggest that glucose starvation may cause a decrease in the NADH:NAD^+ ratio, leading to an increase in the NAD^+:NADH ratio and subsequent production of ROS. By applying flow cytometry analysis with DCFH-DA dye, we demonstrated that ROS production was induced by starvation duration (Fig. 4i). Together, these results provide evidences that glucose starvation can cause an increase in the NAD^+:NADH ratio and lead to the ROS production in the biofilm interior.

ROS can cause oxidation and damage to cell membranes[51,52]. We demonstrated that removing glucose leads to increased damage to the peripheral cell membrane (Fig. 4j), as indicated by Bis-(1,3-dibutylbarbituric acid)pentamethine oxonol (DiBAC4(5)), a dye used to detect membrane damage[51,54]. These findings suggest that glucose starvation in the biofilm interior leads to ROS production and continuous membrane damage; to repair these damaged membranes, the interior bacteria require a continuous supply of FAs from the periphery. Indeed, when FAs were added to the spent medium, the accumulation of intracellular ROS and DiBAC4(5) in the starved bacteria was significantly reduced (Fig. 4k, l), indicating that the membrane was protected. Furthermore, our starvation survival assay showed that the addition of FAs significantly improved the starved bacteria survival compared to the naturally starved group (Fig. 4m, n; Supplementary Fig. 14). The protective effect of FAs was not significant in anaerobic environments (Fig. 4o), indicating again that FAs effectively repair membranes damaged by ROS and help prolong the lifespan of starved bacteria. Cumulatively, by actively exchanging amino acids, with the periphery, the interior bacteria are able to continuously obtain exogenous FAs. This acquisition serves the purpose of repairing the membrane damage caused by ROS resulting from glucose starvation.

Additionally, we speculate that the metabolism and supply of FAs not only affect the survival of the interior bacteria but also impact the overall robustness and antibiotic tolerance of the biofilm. Indeed, when Δ*fabH* biofilms, which are deficient in FAs synthesis, were treated with antibiotics like kanamycin, ciprofloxacin, and ceftazidime, they preferentially collapsed in the interior due to the lack of timely FAs supply (Fig. 5a). On the other hand, in WT biofilm, these antibiotics mainly affected biofilm periphery for an extended period (Fig. 5b), ensuring low antibiotic accumulation in the interior and thereby protecting it[33]. When FAs were supplied to the Δ*fabH* biofilms, the impact of antibiotics had on them was similar to that of WT biofilms (Fig. 5c). This suggests that maintaining a stable FAs supply is crucial for

https://doi.org/10.1038/s41467-024-51940-3

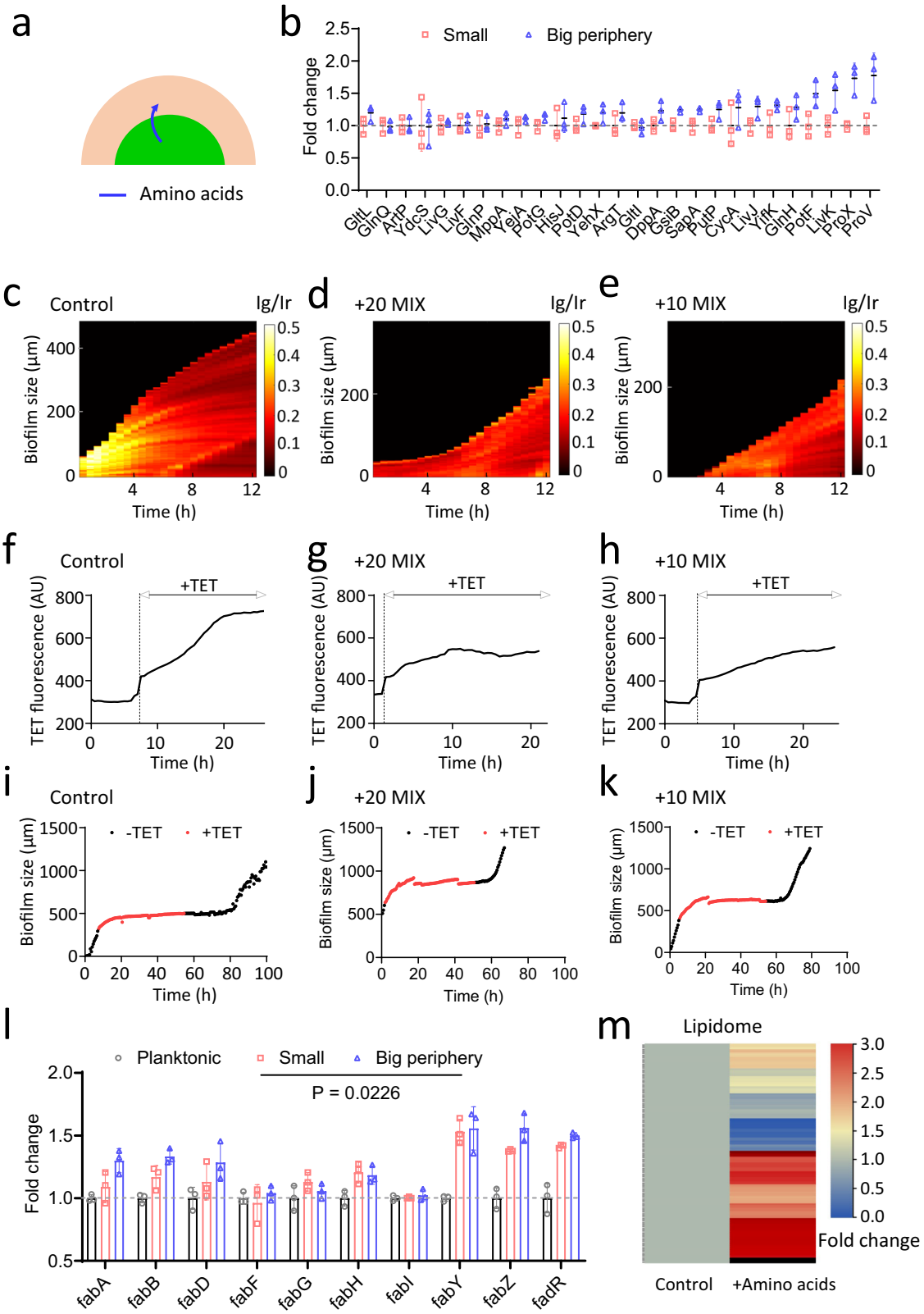

repairing the interior membrane and contributing to sustain antibiotic tolerance in biofilms.

Our findings reveal that nutrient-deprived regions emerge within biofilms due to nutrient gradients, a fundamental aspect of community development. This phenomenon reduces survival capabilities among interior bacteria, while peripheral bacteria, characterized by high membrane potentials and enriched in antibiotics, exhibit lower antibiotic tolerance. To counteract these challenges and enhance their survival and tolerance, interior bacteria supply amino acids to nutrient-rich peripheral bacteria, enabling them to acquire essential FAs crucial for survival. Concurrently, peripheral bacteria reduce de novo amino acid synthesis and membrane potentials, thereby reinforcing antibiotic tolerance. This spatial metabolite exchange allows the resilient periphery of the biofilm to enhance the survival capacity of the interior

https://doi.org/10.1038/s41467-024-51940-3

Fig. 3 | Secretion of amino acids by interior-starved bacteria induces a decrease in peripheral membrane potential and an increase in fatty acid synthesis in biofilm periphery. a Schematic representation illustrating the secretion of interior amino acids to the biofilm periphery. **b** Expression levels of amino acid importer proteins as biofilm size increases. Data are presented as mean values ± SD, 3 biological replicates. Kymographs showing the changes in membrane potential in *E. coli* biofilms under normal M63B1 conditions (**c**) or upon addition of exogenous amino acids (**d**, **e**). The addition of 20 common amino acids at a concentration of 1 mM each is denoted as 20 MIX. The addition of 10 amino acids at a concentration of 2 mM each is denoted as 10 MIX ("Methods" section). **f**–**h** Dynamics of tetracycline (TET, 5 μg/ml) fluorescence in biofilms. The curves are representative of 3 biological replicates. **i**–**k** Growth curves of biofilms before, during, and after treatment with 5 μg/ml TET. The curves are representative of 3 biological replicates. **l** Fold change in fatty acid biosynthesis and degradation as biofilm develops from single cells to community. Data are presented as mean values ± SD, 3 biological replicates. Statistical significance was determined by two-sided Student's *t*-tests: Planktonic vs. Small, *P* value = 0.0072; Small vs. Big-periphery, *P* value = 0.0226. **m** Fold change in lipid content in small biofilms under normal M63B1 conditions (Control) or upon addition of exogenous amino acids (20 MIX). Source data are provided as a Source Data file.

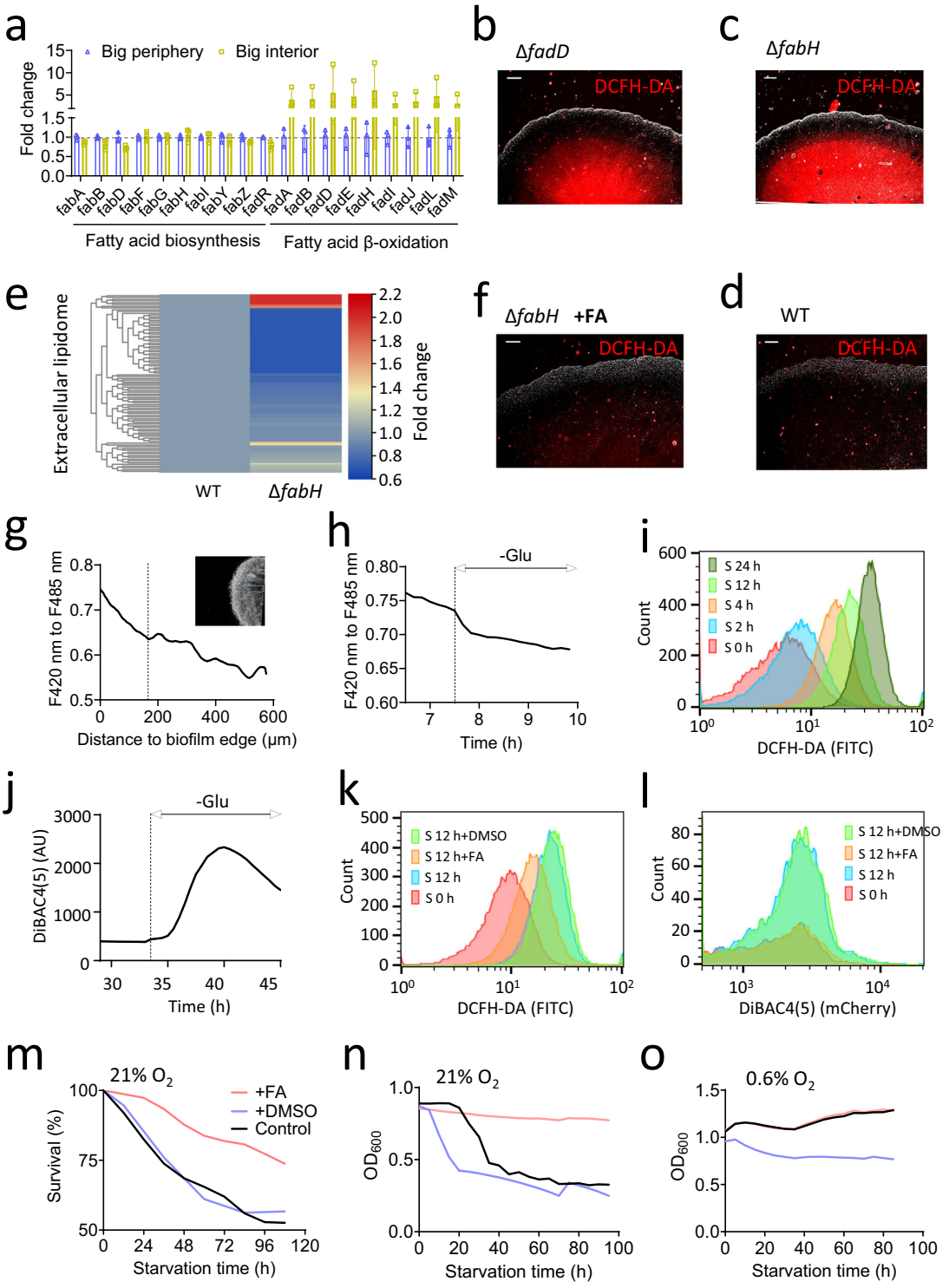

Fig. 4 | Peripheral fatty acids (FAs) supply to biofilm interior enhances survival of starved bacteria by repairing the membrane damage caused by reactive oxygen species (ROS) during starvation. a Fold change in fatty acid biosynthesis and degradation at the periphery and interior of the biofilm. Data are presented as mean values ± SD, 3 biological replicates. Statistical significance was determined by two-sided Student's *t*-tests: *P* value = 0.0024. **b** Distribution of DCFH-DA fluorescence in *ΔfadD* biofilm under normal M63B1 conditions. Composite of phase contrast and DCFH-DA fluorescence (shown in red) channels. Scale bar, 100 μm. Representative of >3 biological replicates. **c** Distribution of DCFH-DA fluorescence in *ΔfabH* biofilm under normal M63B1 conditions. Composite of phase contrast and DCFH-DA fluorescence (shown in red) channels. Scale bar, 100 μm. Representative of >3 biological replicates. **d** Distribution of DCFH-DA fluorescence in wild type (WT) biofilm under normal M63B1 conditions. Composite of phase contrast and DCFH-DA fluorescence (shown in red) channels. Scale bar, 100 μm. Representative of >3 biological replicates. **e** Fold change in extracellular lipids content in WT and *ΔfabH* biofilms. **f** Distribution of DCFH-DA fluorescence in *ΔfabH* biofilm under M63B1 supplemented with 6 μM fatty acids ("Methods" section). Composite of phase contrast and DCFH-DA fluorescence (shown in red) channels. Scale bar, 100 μm. Representative of >3 biological replicates. **g** Distribution of NAD^+:NADH (F420–F485 nm) in WT biofilm. Representative of >3 biological replicates. **h** Decrease in NAD^+:NADH ratio at the biofilm periphery after glucose removal. **i** ROS (determined by DCFH-DA fluorescence) accumulation in planktonic bacteria following different durations of starvation ("Methods" section). **j** Increase in DiBAC4(5) fluorescence at the biofilm periphery after glucose removal. **k**, **l** ROS and membrane damage accumulation (determined by DCFH-DA and DiBAC4(5) fluorescence, respectively) in planktonic bacteria under no starvation (S 0 h), 12 h of starvation (S 12 h), 12 h of starvation with fatty acids added (S 12 h + FA), or 12 h of starvation with DMSO added (S 12 h + DMSO). **m** Survival rate of planktonic bacteria under prolonged starvation in an aerobic environment. **n** Optical Density at 600 nm (OD_{600}) measurements of planktonic bacteria under prolonged starvation in an aerobic environment. Two biological replicates. **o** OD_{600} measurements of planktonic bacteria under prolonged starvation in an anaerobic environment. Two biological replicates. Source data are provided as a Source Data file.

bacteria, which, in turn, with their innate strong antibiotic tolerance, bolster the periphery's ability to withstand antibiotics. Ultimately, this synergistic interaction leads to an overall enhancement in the biofilm's survival and tolerance (Fig. 5d).

Discussion

Our findings reveal the evolution of sophisticated collective behaviors within biofilms, distinguishing them from individual organisms and enhancing their resilience. By understanding these mechanisms, we gain insights into the evolutionary success of biofilms. Moreover, this knowledge enables us to devise novel strategies to combat biofilm infections, such as targeting FA synthesis or implementing combination approaches to improve membrane potential and drug accumulation. Additionally, this work highlights the contribution of spatial metabolite exchange to biofilm collective behavior and enhanced abilities. However, it is evident that it lacks a comprehensive understanding and discussion of the molecular regulatory mechanisms underlying these macroscopic material exchanges. Further research and discussion are needed to delve into this aspect.

The common intuition is that growth arrest in starved bacteria is a result of insufficient raw materials rather than their abundance. Interestingly, here we found that interior-starved bacteria, despite being growth-stalled, actually serve as suppliers of external amino acids. It remains unclear why amino acids become abundant when biofilm growth halts due to glucose starvation. One possible explanation is that the starvation experienced within the biofilm's interior is more akin to sudden starvation, particularly in the region near the 2-NBDG band, which corresponds to the critical glucose concentration that determines growth. In this region, bacteria transition abruptly from a growing state to a non-growing state. Existing literature[55] suggests that sudden starvation causes significant termination of protein translation and DNA replication but no change in other genes, which may lead to an increase and accumulation of intracellular free amino acids.

Our findings echo previous research[33] wherein peripheral lipid synthesis is jointly and exclusively activated, treated with seven different antibiotics, and lipid synthesis is responsible for the continuous glucose consumption at the biofilm periphery. However, fundamental questions regarding why lipid synthesis is activated, how biofilms can maintain stable lipid synthesis at the periphery, and what the significance of lipid activation is, remained unanswered until this work. Now, the above questions seem to be answered. First, FA and main amino acid synthesis pathways share a common precursor, Acetyl-CoA. When growth ceases due to antibiotic treatment, protein translation is blocked, resulting in increased intracellular free amino acids (Fig. 2h). Then the amino acid synthesis pathway weakens (Fig. 2e), which may lead to an enhanced FA synthesis from Acetyl-CoA. Of course, all of these events are based on the premise that the conversion ability of glucose to Acetyl-CoA has not decreased[33]. Second, the significance of lipid synthesis activation is evidenced by the need for peripheral bacteria to repair membrane damage or supply FAs to the interior. We believed that the latter carries more weight in this case. Figure 5 suggests that if the peripheral FAs synthesis is impaired (Δ*fabH*), the impact of antibiotics on the interior is greater than that on the periphery, although antibiotics are distributed in the periphery. However, as long as FAs are added to the medium, the antibiotic tolerance in the Δ*fabH* biofilm is close to that in the WT biofilm. Therefore, the interior demand for FAs is more important for their survival. Under conditions of no external additives, obtaining FAs from the periphery through metabolite exchange appears to be the most feasible solution.

Methods

Microfluidic chip fabrication

We designed and manufactured the microfluidic chip in-house[28]. To fabricate master mold of the microfluidic chip, we used the Maskless Mold Fabrication Method from BlackHole Lab (France). For lithography procedures, we performed a photoresist from Microchemicals (AZ4562) on glass or silicon slides. We prepared the polydimethylsiloxane (PDMS) by pouring a 10:1 (v/v) mixture of Sylgard 184 elastomer and curing agent (Dow Corning, USA) on the master mold, and cured the mixture for 2 h in an oven at 80 °C. Then, we peeled the cured PDMS with chamber pattern off from the mold and punched with holes at the inlet and outlet ports. We created the bacterial loading zone with the method as described before[28]. Then, we bounded the PDMS immediately with a glass slide or with a PDMS layer with a thickness of 1 mm (Fig. 2d, spatial multi-omics chip). Finally, we plugged the inlet and outlet ports by using syringe needles (20G, 0.91 mm OD × 0.61 mm ID) and PTFE Tubing (1/16″ OD × 1/32 ID).

Cultivation of biofilms using the microfluidic system

The bacterial strains used in this study are *E. coli* BW25113 (Supplementary Table 1). The day before the experiment, we streaked the bacteria from −80 °C glycerol stock on LB agar plates and incubated at 37 °C overnight. On the next day, we picked a single colony from the plate, inoculated the bacteria to 5 ml of LB broth in a 50 ml conical tube, and incubated them at 37 °C in a shaker. After a 12-h incubation period, we centrifuged the culture at a relative centrifugal force of 7000 × *g* for 3 min. We then resuspended the pellet in 0.5 ml of PBS buffer, serving as the loading culture for the microfluidics system. In the experiments performed by microfluidic system, we used Elveflow OB1 Mk3 Pressure Controller (ELVESYS, France) to drive flow of the growth medium. Initially, to prevent the

https://doi.org/10.1038/s41467-024-51940-3

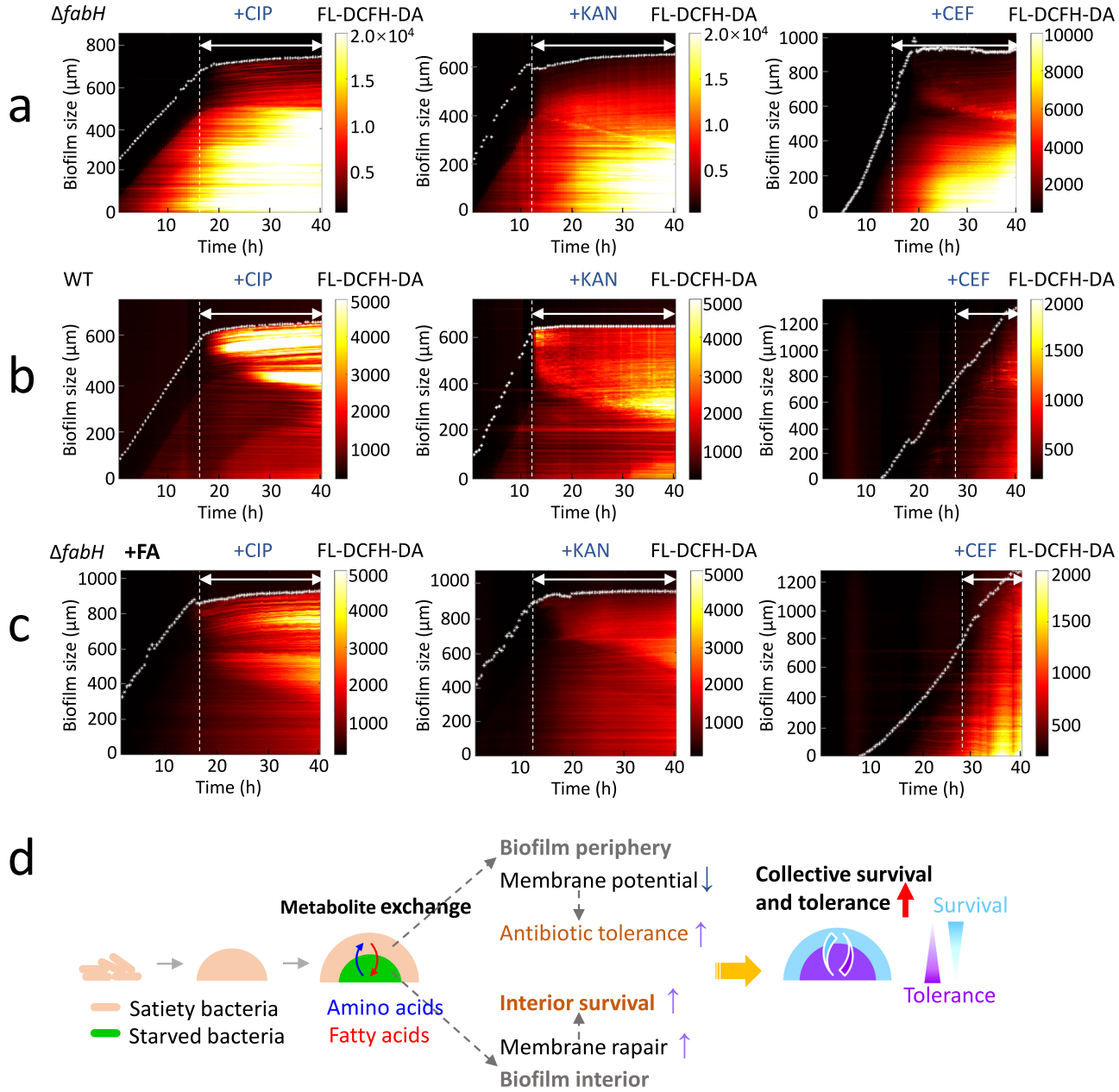

Fig. 5 | The extensive protective effect of fatty acids (FAs) on starving bacteria. Kymograph showing the accumulation of DCFH-DA fluorescence in biofilms of in Δ*fabH* (**a**), WT (**b**), and Δ*fabH* (**c**) strains before and after the addition of different antibiotics. The following antibiotic concentrations were used: 0.06 μg/ml ciprofloxacin (CIP), 10 μg/ml kanamycin (KAN), and 4 μg/ml ceftazidime (CEF). In the case of the Δ*fabH* biofilm (**c**), an initial concentration of 6 μM fatty acids (FAs) (see "Methods" section) was added to the medium. **d** Theoretical model depicting spatial metabolite exchange within a biofilm community, explaining the improvement in survival and enhancement of drug tolerance. Source data are provided as a Source Data file.

adhesion of individual bacteria during loading, we treated the surface of the microfluidic chamber with 5% BSA (bovine serum albumin) solution for 30 min. Subsequently, we switched the buffer in the chamber back to PBS. Then, we loaded the bacterial culture in PBS into the microfluidic chip, until we trapped 1000 bacterial cells approximately at the seeding zone. During the rest of the experiment, we fed the growth chamber with biofilm medium under a constant pressure of 3 psi; this pressure resulted in a flow rate of 400 μm/s, which in our experience was sufficient to maintain a clean growth chamber and enabled long-term observation of the biofilm. The temperature was kept at 37 °C. This pressure yielded a flow rate of 400 μm/s, which, based on our prior experiences, proved adequate for sustaining a pristine growth chamber and facilitating prolonged observation of the biofilm.

Culture medium

In this paper, we used M63B1 medium to culture *E. coli* biofilms: 100 mM KH_2PO_4, 15 mM $(NH4)_2SO_4$, 0.8 mM $MgSO_4$, 3 μM vitamin B1, 22 mM glucose, adjusted to pH 7.4 with KOH. In the nutrient removal experiments, we switched M63B1 medium to M63B1 without glucose. The concentrations of antibiotics and reagents applied throughout this study, unless expressly specified, were as follows: 25 μg/ml tetracycline (Solarbio Life Sciences), 50 μg/ml kanamycin (Sigma-Aldrich), 20 μg/ml ceftazidime (Sigma-Aldrich), 0.6 μg/ml ciprofloxacin (Solarbio Life Sciences), 10 μm 2-[*N*-(7-nitrobenz-2-oxa-1,3-diazol-4-yl) amino]-2-deoxy-D-glucose (2-NBDG), (Targetmol), 5 μm DCFH-DA (Targetmol), and 500 nM DiBAC4(5) (Life Technologies). The addition of 20 common amino acids (Alanine, Valine, Leucine, Isoleucine, Proline, Serine, Phenylalanine, Tryptophan, Threonine, Tyrosine,

Aspartic acid, Glutamic acid, Glutamine, Lysine, Arginine, Histidine, Glycine, Cysteine, Methionine, and Asparagine) at a concentration of 1 mM each is denoted as 20 MIX. The addition of ten amino acids (Lysine, Glutamate, Methionine, Glutamine, Glycine, Cysteine, Phenylalanine, Tryptophan, Tyrosine and Histidine), referring to the top ten amino acids in Fig. 2f, at a concentration of 2 mM each is denoted as 10 MIX.

Microscopy

We observed the biofilms with phase contrast and fluorescence microscopy. Initially, we equipped the Olympus IX83 microscope (Japan) with Andor's Zyla 4.2 sCMOS camera (UK) to serve as our primary imaging system. We used a 10× objective lens in most of the experiments to image the entire biofilm and took images every 20–30 min. For confocal microscopy experiments, we observed and recorded using an inverted Zeiss LSM 710 three-channel laser scanning microscope (Carl-Zeiss)[56]. Tetracycline fluorescence was excited at 405 nm and detected at 520–550 nm.

Interior and periphery bacteria extraction from the biofilm

We cultured *E. coli* cells in standard M63B1 medium at 37 °C in our omics chip (L × W × H = 30 mm × 6 mm × 100 μm). Before bacteria extraction from the biofilm, we switched the medium to M63B1 containing 33 μM 2-NBDG for proteomics and metabolomics studies. For transcriptomics studies, we switched the cultivation medium to RNA-later reagent (RNA Stabilization Solution, Invitrogen™, AM7021) containing 33 μM 2-NBDG. Subsequently, we swiftly and manually dissected the chip with a scalpel to separate the interior and periphery parts of the biofilm along the 2-NBDG band under a stereofluoroscope. Subsequently, we rapidly rinsed the bacteria with pre-chilled 4 °C PBS. The number of bacterial cells in the biofilm reached 100 million, and the total protein amount extracted from a single biofilm was ~50 μg. Cell number and protein amount enabled sample preparation in metabolomics, transcriptomics and proteomics studies.

Proteomics sample preparation

We collected planktonic cells (OD_{600}≈0.2), biofilm interior, and periphery samples through centrifugation at 13,000 × *g* at 4 °C. Then we washed these samples twice with 200 μl ice-cold PBS buffer and separated supernatant and bacteria cells by centrifugation at 13,000 × *g*. We resuspended bacterial cells in 100 μl lysis buffer (1% sodium deoxycholate, pH = 8.0, 20 mM Tris-HCl) and heated the mix to 90 °C for 10 min. Subsequently, we disrupted the samples by strong vortexing and indirect sonication (100% amplitude, 45 s on, 30 s off, 20 cycles) by using a Bioruptor Pico 2020. We centrifuged the *E. coli* lysates at 16,000 x *g* for 15 min at 4 °C to remove cellular debris. After centrifugation, we collected the supernatants and determined the protein concentration by bicinchoninic acid assay (BCA kit, Thermo Fisher Scientific). We froze the protein extracts in liquid nitrogen and stored them at −80 °C until use. Then, we diluted the samples with lysis buffer to a final protein concentration of 0.5 mg/ml. We reduced the proteins obtained from the different samples with 5 mM TCEP for 60 min at 37 °C and alkylated with 10 mM iodoacetamide for 30 min in the dark at 25 °C. After quenching the reaction with light exposure for 20 min at 25 °C, we further digested the samples by trypsin overnight at 37 °C and quenched them by adding wash buffer (100% 2-isopropanol, 1% trifluoroacetic acid) to four times their original volume. Finally, we loaded the peptide mixtures onto SDB-Rps cartridges (Empore) and desalted the mixtures as described before[57].

DDA peptide pre-fractionation and spectral library generation

For LC–MS/MS data dependent acquisition (DDA) peptides fraction, we used HPLC (XBridge™ BEH300 C18 column (Waters, MA)) to reduce sample complexity. In the process of HPLC fractionation, buffer A was H_2O adjusted by $NH_3{\cdot}H_2O$ to pH = 10 and buffer B was 98% acetonitrile adjusted by $NH_3{\cdot}H_2O$ to pH = 10. We ionized and detected the eluted peptides with an Orbitrap Fusion LUMOS Tribrid mass spectrometer (Thermo Fisher Scientific) and isolated pcursor peptides with 33 variable windows spanning from 350 to 1650 m/z at resolution = 30,000. We analyzed all the raw files by Spectronaut 15.6 software and generated a spectral library (contains 2923 *E. coli* proteins, 32,491 peptide sequences) by DDA results with the search against Uniprot *E. coli* database (downloaded at 2021/07/01). Our DDA database consists of 2923 *E. coli* proteins, resulting in a total of 32,491 protein sequences.

DIA data acquisition

For DIA analysis, we solubilized the samples in 0.1% trifluoroacetic acid at a concentration of 1 μg/μl. Subsequently, we mixed 5 μl samples with 1.2 μl 1*iRT reagent (Biognosys iRT Kit, Ki-3002-1) and 1.8 μl 0. 1% trifluoroacetic acid. Here, we used indexed retention time (iRT) reagent to normalize the retention time of peptides in all samples[58]. Finally, we injected 5 μl of the mix per LC–MS/MS run. For peptide separation, we performed the experiments on a (75 μm × 45 cm) packed in-house with C18 resin (ReprosilAQ Pur, Dr. Maisch 1.9 μm) using a linear gradient from 95% solvent A (98% water, 2% acetonitrile, 0.1% trifluoroacetic acid) and 5% solvent B (98% acetonitrile, 2% water, 0.1% trifluoroacetic acid) to 30% solvent B over 120 min at a flow rate of 0.3 μl/min. For DIA sample measurements, we acquired 20 variable-width DIA isolation windows recursively. The DIA isolation setup included a 1 m/z overlap between windows, as described in previous research[59]. We acquired the DIA-MS2 spectra at a resolution of 15,000 and an automatic gain control (AGC) target of 1×10^5. Using our DDA libraries, we performed targeted data extraction of DIA-MS acquisitions with Spectronaut (Biognosys AG, version 13) with default settings. To calculate the ideal mass tolerances for data extraction, we applied the dynamic mass tolerance strategy and no correction factor (correction factor = 1). To obtain the relative quantitative data, we normalized and statistically analyzed the data by using Spectronaut® Software[60], then classified them according to Clusters of Orthologous Genes (COGs)[61,62].

Transcriptomics sample preparation and analysis

We adopted our previously established method MiniBac-seq[25] to prepare RNA-seq library. In brief, after cell acquisition, we centrifuged the sample at 5000 × *g* for 15 min to discard the supernatant. The cell pellet was resuspended with 50 μl of TE (10 mM Tris and 1 mM disodium EDTA) buffer (pH 8.0, Thermo Fisher Scientific, AM9849) containing 12.5 mg/ml lysozyme (Sigma-Aldrich, 62970-1G-F) and 16.7% (v:v) Proteinase K (Qiagen, 19131), incubated at 37 °C for 15 min on a shaker at 500 r.p.m. Bacterial RNA was then purified using RNAClean XP beads (Beckman, A63987).

After purifying the total RNA, contaminant DNA was depleted with DNase I treatment. rRNA plus non-coding element ssrA was further removed with the customized ssDNA library. Next, RT was carried out (Thermo Fisher Scientific, EP0753), and the molecular barcode embedding in RT primer was introduced to each sample. Six samples were pooled together after RT and subjected to purification. Second-strand synthesis was subsequently performed with NEBNext Second Strand Synthesis Kit (New England Biolabs, E6111S). Purified double-strand cDNA was further tagmented with N7 adapter-incubating transposase (Vazyme, TD513) and PCR amplified with around 15 cycles to a final product of around 50 ng. We confirmed that the amplification stops at the exponential phase. We quantified the product using Qubit dsDNA HS Kit (Thermo Fisher Scientific, Q32854) and the insert size distribution using Bioanalyzer 2100 (Agilent). A thermocycler was used in our protocol when necessary (Bio-Rad, T100). The library passing quality control was subjected to sequencing by GENEWIZ via Illumina NovaSeq 6000 system with 2 × 150 paired-end configuration. We got one million paired-end reads for each sample.

The raw data were first subjected to FastQC (version 0.11.9) and quality trimming (cutadapt, version 2.10). We next demultiplexed the

data according to the first seven nucleotides anchored at the 5′ end from the first read. Internal adapter sequence embedding in some second reads with too short insert (<150 bp) was also trimmed subsequently. We further filtered out both the first and second reads with a minimum length threshold of 20 bp. Subsequently, we aligned the second read to a reference genome (NC000913.3) (bowtie2, version 2.4.1). The R method summarizeOverlaps from the GenomicAlignments package (version 1.26.0) was used in feature counting in a strand-specific manner, giving rise to a read count table for each gene. Finally, we calculated the TPM value for each gene after excluding the rRNA reads.

Metabolomics sample preparation and analysis

Samples for metabolomics analysis were collected, washed, and harvested with the same processes as for the proteomics samples described above. For extracellular metabolomics, the supernatant was rapidly placed on ice and mixed with 400 µl of 80% (vol/vol) methanol (pre-chilled to −80 °C) for 4 h, then centrifuged at 14,000 × *g* for 20 min at 4–8 °C and the supernatant was transferred to a new 1.5-ml tube on dry ice. For intracellular metabolomics, bacteria cells were rapidly placed on ice and mixed with 400 µl of 80% (vol/vol) methanol (pre-chilled to −80 °C). Intracellular metabolites were then extracted using sonication (100% amplitude, 20 cycles of 45 s on 30 s off) in Bioruptor Pico 2020. The resulting lysate was incubated at −80 °C for 2 h or overnight, then centrifuged at 14,000 × *g* for 20 min at 4–8 °C and the supernatant was transferred to a new 1.5-ml tube on dry ice. The supernatants were then quantified using a Q Exactive™ Plus Orbitrap mass spectrometer (Thermo Fisher) with Ultimate 3000 Ultra High-Performance Liquid Chromatography (HPLC, Dionex Corporation of America). Protein concentrations in each sample were measured to perform normalization of metabolite abundance.

Lipidomics sample preparation and analysis

For lipidomics analyses, we collected, washed, and harvested the bacteria cells with the same processes as proteome samples described above. We extracted total FAs from bacteria cells by chloroform/methanol (2:1 vol/vol) as previously described[63]. Then, we desiccated the collected FAs through a gentle stream of nitrogen[64] and resuspended by 50 µl chloroform/isopropanol (2:8 vol/vol). To inject and separate lipid samples, we integrated Ultimate 3000 Ultra HPLC (Dionex Corporation of America) with Q Exactive Plus High-Resolution Mass Spectrometry (Thermo Fisher Scientific, ACQUITY UPLC BEH C18 Column, 2.1 × 100 mm, 1.7 µm). For HPLC separation, buffer A was 60% acetonitrile–40%H_2O–10 mM NH_4Ac–0.1% formic acid and buffer B was 80% isopropanol–20% acetonitrile–10 mM NH_4Ac–0.1% formic acid. Then, we carried out the electrospray ionization by positive ion mode (spray voltage +3.2 kV) and negative ion mode (spray voltage −3.0 kV). For the MS1 full scan, we acquired ions with m/z ranging from 100 to 1500 by Thermo Q Exactive mass analyzer at a high resolution of 70,000. The AGC was 10^6 and the maximal ion injection time of full MS was 100 ms. MS2 acquisition was at 17,500 resolution and an AGC of 10^5. The maximal ion injection time of MS2 was 50 ms. Finally, we measured the protein concentration in each sample as normalization of metabolites abundance.

^{13}C flux sample preparation and analysis

M63B1 medium with [U-$^{13}C_6$]-D-glucose was used in the ^{13}C labeling experiments. First, we inoculated and cultivated the biofilm in standard M63B1. While we added antibiotics to treat biofilms in microfluidic chip, the medium was replaced by 100% [U-$^{13}C_6$]-D-glucose M63B1. Control samples were treated by changing to 100% [U-$^{13}C_6$]-D-glucose M63B1 and cultivated at the same time as the antibiotics treated group[65]. The cells were collected, washed, then resuspended into 80% (w/w) cold methanol, and disrupted in the same way as proteome samples. ^{13}C labeling experiments samples, were analyzed on a Q Exactive™ Plus Orbitrap mass spectrometer (Thermo Fisher) with Ultimate 3000 Ultra HPLC (Dionex Corporation of America). A Waters BEH Amide Column (2.1 × 100 mm, 1.7 µm) was used for HPLC separation. Buffer A was acetonitrile–0.1% formic acid and buffer B was water–10 mM NH_4Ac–0.1% formic acid. HPLC gradient was 30 min (0–5 min, 0% of buffer B; 5–6 min, 0%–25% of buffer B; 6–15 min, 25% of buffer B; 15–16 min, 25%–50% of buffer B; 16–25 min, 50% of buffer B; 25–26 min, 50%–0% of buffer B; 26–30 min, 0% buffer B) at a flow rate of 0.3 ml/min. Electrospray ionization was carried out by positive ion mode (spray voltage +3.2 kV) and negative ion mode (spray voltage −3.0 kV). For the MS1 full scan, ions with m/z ranging from 70 to 1000 were acquired by Orbitrap mass analyzer at a high resolution of 70,000. The AGC was set as 10^6. The maximal ion injection time of full MS was 100 ms. MS2 acquisition was performed at 17,500 resolution and an AGC of 10^5. Precursor ions were selected and fragmented with higher energy collision dissociation with normalized collision energy of 30–40–50%. The maximal ion injection time of MS2 was 50 ms[63]. Raw data were processed using Mzvault 2.2 database (Thermo Fisher) and Xcalibur Qual Browser (Thermo Fisher). For each scan mode, metabolite identities were confirmed using authentic reference standards from IROA Technologies Company. Metabolite molecular formulas matching to within 5 parts per million were selected as candidate identifiers. Identification of unknown compounds using compound discovery 3.2, mzcloud, and mzVault databases[66].

Antibiotic survival assay

To obtain seed culture, we inoculated the bacteria at LB medium from an overnight culture. Then, we added 4 µL of the seed culture into 200 µL of fresh M63B1 medium and incubated in 96-well plates. When the cells grown to log phase (OD600 ≈ 0.2), antibiotics were added and treated for 1, 3, 6, 9, 12, 15, 20, and 24 h. We washed and serially diluted the cultures with PBS and plated them onto M63B1 agar. After 36 h cultivated in a 37 °C incubator, we counted bacteria numbers on plates. Among all colony forming unit (CFU) experiments, we performed them with biological replicates from independent cultures.

Flow cytometry

To validate tetracycline enrichment in bacteria dependent on membrane potential or not, we compared the tetracycline accumulation in planktonic bacteria with 20 µm CCCP added or not. We performed in V500-A channel on a FACS Aria SORP (BD Biosciences). After growth to mid-exponential phase (OD_{600} ≈ 0.3) in SPARK microplate reader, the cultures were treated under 2 µg/ml TET with or without 20 µm CCCP for 4 h. Then, we chilled the samples with or without TET on ice immediately and diluted in 1 ml of pre-chilled PBS. A 500-fold dilution was applied to each sample, making them appropriate samples for flow cytometry experiments.

To measure intracellular ROS intensity and cell membrane damage during starvation, we used the FITC (DCFH-DA) and mCherry channel (Dibac4(5)) on FACS Thermo Bigfoot (Invitrogen). We used a blank *E. coli* BW25113 strain as a negative control in the primary cytometry setting. After growth to late-stationary phase (30 h after seeding) in SPARK microplate reader, we collected spent medium by centrifugation at 13,000 × *g* at 4 °C. Then, we collected exponential-stage *E. coli* (OD_{600} ≈ 0.3) by centrifugation at 13,000 × *g* at 4 °C and resuspended by same volume fresh medium (M63B1), spent medium and spent medium with 150 µl FA stock or DMSO as control. To obtain bacterial FA stock, we extracted total FAs from cell cultures (5 mL exponential-stage and stationary-stage *E.coli*) by chloroform/methanol (2:1 vol/vol) as previously described. Then, we desiccated the collected FAs through a gentle stream of nitrogen and resuspended by 150 µl DMSO. For ROS intensity and cell membrane damage measurement, we used 10 µM DCFH-DA and 500 nM DiBAC4(5) in the resuspended medium. After 12 h of incubation at 37 °C in a shaker, the samples were immediately put on ice and diluted in 1 ml of pre-chilled PBS. For

subsequent flow cytometry analysis, we prepared each sample with a 500-fold dilution.

Starvation survival assay

To obtain seed culture, we inoculated the bacteria at LB medium from an overnight culture. For the aerobic experiment (21% O_2), we added 4 µL of the seed culture into 200 µL of fresh M63B1 medium, M63B1 medium with 150 µl FA stock or DMSO and incubated in 96-well plates. After 16 h of seeding, the cells grown to stationary phase, we began to record the survival curve by OD_{600} for 100 h approximately. For CFU experiments, we collected cultures with different starvation time, then washed and serially diluted the cultures with PBS and plated them onto M63B1 agar. After 36 h cultivated in a 37 °C incubator, we counted bacteria numbers on plates. Among all CFU experiments, we performed them with biological replicates from independent cultures. For the anaerobic starvation experiment (0.6% O_2), we followed a similar procedure. After the bacteria reached the stationary phase under aerobic conditions, we created a low oxygen environment using N_2 in the microplate reader. Subsequently, we initiated the recording of the survival curve by measuring the OD_{600}.

Image analysis

For data analysis, we used ImageJ (1.53q, National Institutes of Health, USA) and MATLAB (R2019a, MathWorks, USA). We used ImageJ to prepare the snapshots of the biofilms and MATLAB to calculate biofilm expansion and fluorescence profiles in the biofilms. To detect region of expansion in a biofilm, we performed image differencing on snapshots of the biofilm from time-lapse microscopic images[67]. Specifically, we compared the difference between two consecutive phase contrast images by calculating the absolute difference between corresponding pixels in the two images. Since expansion leads to pixel level changes and no expansion leads to little change, imDiff could reveal the growth zone in the biofilm.

Statistical analysis

In the figures, we performed two-tailed Student's *t*-tests for data analysis and presented each value as the mean derived from a minimum of 3 biological replicates (refer to the legend for specific replicate numbers), with standard deviation represented by error bars. For biofilm samples, biological replicates referred to biofilms cultivated in independent chambers.

Reporting summary

Further information on research design is available in the Nature Portfolio Reporting Summary linked to this article.

Data availability

All data are available in the main text or the Supplementary Materials. The RNA-seq data have been deposited in the NCBI SRA database under accession code PRJNA1149552; The proteomic mass spectrometry raw data have been deposited in the ProteomeXchange partner database under accession code MSV000095638; The lipidomic and metabolomic mass spectrometry raw data have been deposited in the MassIVE database under accession code MSV000095639. Source data are provided with this paper.

References

1. Lyons, N. A. & Kolter, R. On the evolution of bacterial multicellularity. *Curr. Opin. Microbiol.* **24**, 21–28 (2015).
2. Hall-Stoodley, L., Costerton, J. W. & Stoodley, P. Bacterial biofilms: from the Natural environment to infectious diseases. *Nat. Rev. Microbiol.* **2**, 95–108 (2004).
3. Arnaouteli, S., Bamford, N. C., Stanley-Wall, N. R. & Kovács, Á. T. Bacillus subtilis biofilm formation and social interactions. *Nat. Rev. Microbiol.* **19**, 600–614 (2021).
4. Nadell, C. D., Drescher, K. & Foster, K. R. Spatial structure, cooperation and competition in biofilms. *Nat. Rev. Microbiol.* **14**, 589–600 (2016).
5. Sauer, K. et al. The biofilm life cycle: expanding the conceptual model of biofilm formation. *Nat. Rev. Microbiol.* **20**, 608–620 (2022).
6. Meredith, H. R., Srimani, J. K., Lee, A. J., Lopatkin, A. J. & You, L. Collective antibiotic tolerance: mechanisms, dynamics and intervention. *Nat. Chem. Biol.* **11**, 182–188 (2015).
7. Ibberson, C. B., Barraza, J. P., Holmes, A. L., Cao, P. & Whiteley, M. Precise spatial structure impacts antimicrobial susceptibility of *S. aureus* in polymicrobial wound infections. *Proc. Natl Acad. Sci. USA* **119**, e2212340119 (2022).
8. Davies, D. Understanding biofilm resistance to antibacterial agents. *Nat. Rev. Drug Discov.* **2**, 114–122 (2003).
9. Stewart, P. S. & Costerton, J. W. Antibiotic resistance of bacteria in biofilms. *Lancet* **358**, 135–138 (2001).
10. Flemming, H.-C. & Wingender, J. The biofilm matrix. *Nat. Rev. Microbiol.* **8**, 623–633 (2010).
11. Ciofu, O., Moser, C., Jensen, P, Ø. & Høiby, N. Tolerance and resistance of microbial biofilms. *Nat. Rev. Microbiol.* **20**, 621–635 (2022).
12. Parsek, M. R. & Singh, P. K. Bacterial biofilms: an emerging link to disease pathogenesis. *Annu. Rev. Microbiol.* **57**, 677–701 (2003).
13. Smith, W. P. J., Wucher, B. R., Nadell, C. D. & Foster, K. R. Bacterial defences: mechanisms, evolution and antimicrobial resistance. *Nat. Rev. Microbiol.* **21**, 519–534 (2023).
14. Teschler, J. K. et al. Living in the matrix: assembly and control of Vibrio cholerae biofilms. *Nat. Rev. Microbiol.* **13**, 255–268 (2015).
15. Nadell, C. D., Ricaurte, D., Yan, J., Drescher, K. & Bassler, B. L. Flow environment and matrix structure interact to determine spatial competition in *Pseudomonas aeruginosa* biofilms. *eLife* **6**, e21855 (2017).
16. Anderl, J. N., Franklin, M. J. & Stewart, P. S. Role of antibiotic penetration limitation in *Klebsiella pneumoniae* biofilm resistance to ampicillin and ciprofloxacin. *Antimicrob. Agents Chemother.* **44**, 1818–1824 (2000).
17. Rodríguez-Martínez, J. M., Ballesta, S. & Pascual, A. Activity and penetration of fosfomycin, ciprofloxacin, amoxicillin/clavulanic acid and co-trimoxazole in *Escherichia coli* and *Pseudomonas aeruginosa* biofilms. *Int. J. Antimicrob. Agents* **30**, 366–368 (2007).
18. Zheng, Z. & Stewart, P. S. Penetration of rifampin through Staphylococcus epidermidis biofilms. *Antimicrob. Agents Chemother.* **46**, 900–903 (2002).
19. Xavier, J. B. & Foster, K. R. Cooperation and conflict in microbial biofilms. *Proc. Natl Acad. Sci. USA* **104**, 876–881 (2007).
20. Pontrelli, S. et al. Metabolic cross-feeding structures the assembly of polysaccharide degrading communities. *Sci. Adv.* **8**, eabk3076 (2022).
21. Wu, Y. et al. Cooperative microbial interactions drive spatial segregation in porous environments. *Nat. Commun.* **14**, 4226 (2023).
22. Olin-Sandoval, V. et al. Lysine harvesting is an antioxidant strategy and triggers underground polyamine metabolism. *Nature* **572**, 249–253 (2019).
23. Blasche, S. et al. Metabolic cooperation and spatiotemporal niche partitioning in a kefir microbial community. *Nat. Microbiol.* **6**, 196–208 (2021).
24. Yu, J. S. L. et al. Microbial communities form rich extracellular metabolomes that foster metabolic interactions and promote drug tolerance. *Nat. Microbiol.* **7**, 542–555 (2022).
25. Wang, T., Shen, P., He, Y., Zhang, Y. & Liu, J. Spatial transcriptome uncovers rich coordination of metabolism in *E. coli* K12 biofilm. *Nat. Chem. Biol.* **19**, 940–950 (2023).
26. Díaz-Pascual, F. et al. Spatial alanine metabolism determines local growth dynamics of *Escherichia coli* colonies. *eLife* **10**, e70794 (2021).

27. Jeckel, H. et al. Simultaneous spatiotemporal transcriptomics and microscopy of *Bacillus subtilis* swarm development reveal cooperation across generations. *Nat. Microbiol.* **8**, 2378–2391 (2023).
28. Zhang, Y. et al. A microfluidic approach for quantitative study of spatial heterogeneity in bacterial biofilms. *Small Sci*. 2200047 https://doi.org/10.1002/smsc.202200047 (2022).
29. Chalabaev, S. et al. Biofilms formed by gram-negative bacteria undergo increased lipid A palmitoylation, enhancing in vivo survival. *mBio* **5**, e01116–14 (2014).
30. Yoshioka, K. et al. A novel fluorescent derivative of glucose applicable to the assessment of glucose uptake activity of *Escherichia coli*. *Biochim. Biophys. Acta* **1289**, 5–9 (1996).
31. Yoshioka, K. et al. Intracellular fate of 2-NBDG, a fluorescent probe for glucose uptake activity, in *Escherichia coli* cells. *Biosci. Biotechnol. Biochem.* **60**, 1899–1901 (1996).
32. Dal Co, A., Ackermann, M. & van Vliet, S. Metabolic activity affects the response of single cells to a nutrient switch in structured populations. *J. R. Soc. Interface* **16**, 20190182 (2019).
33. Zhang, Y. et al. Persistent glucose consumption under antibiotic treatment protects bacterial community. *Nat. Chem. Biol*. https://doi.org/10.1038/s41589-024-01708-z (2024).
34. Bryan, L. E. & Kwan, S. Roles of ribosomal binding, membrane potential, and electron transport in bacterial uptake of streptomycin and gentamicin. *Antimicrob. Agents Chemother.* **23**, 835–845 (1983).
35. Bryan, L. E. & Van Den Elzen, H. M. Effects of membrane-energy mutations and cations on streptomycin and gentamicin accumulation by bacteria: a model for entry of streptomycin and gentamicin in susceptible and resistant bacteria. *Antimicrob. Agents Chemother.* **12**, 163–177 (1977).
36. Argast, M. & Beck, C. F. Tetracycline uptake by susceptible *Escherichia coli* cells. *Arch. Microbiol.* **141**, 260–265 (1985).
37. McMurry, L. M., Cullinane, J. C., Petrucci, R. E. & Levy, S. B. Active uptake of tetracycline by membrane vesicles from susceptible *Escherichia coli*. *Antimicrob. Agents Chemother.* **20**, 307–313 (1981).
38. Jin, X. et al. Sensitive bacterial V_m sensors revealed the excitability of bacterial V_m and its role in antibiotic tolerance. *Proc. Natl Acad. Sci. USA* **120**, e2208348120 (2023).
39. Werley, C. A., Boccardo, S., Rigamonti, A., Hansson, E. M. & Cohen, A. E. Multiplexed Optical Sensors in Arrayed Islands of Cells for multimodal recordings of cellular physiology. *Nat. Commun.* **11**, 3881 (2020).
40. Rosenberg, M., Azevedo, N. F. & Ivask, A. Propidium iodide staining underestimates viability of adherent bacterial cells. *Sci. Rep.* **9**, 6483 (2019).
41. Abisado, R. G., Benomar, S., Klaus, J. R., Dandekar, A. A. & Chandler, J. R. Bacterial quorum sensing and microbial community interactions. *mBio* **9**, e02331–17 (2018).
42. Mukherjee, S. & Bassler, B. L. Bacterial quorum sensing in complex and dynamically changing environments. *Nat. Rev. Microbiol.* **17**, 371–382 (2019).
43. Meylan, S. et al. Carbon sources tune antibiotic susceptibility in *Pseudomonas aeruginosa* via tricarboxylic acid cycle control. *Cell Chem. Biol.* **24**, 195–206 (2017).
44. Kaila, V. R. I. & Wikström, M. Architecture of bacterial respiratory chains. *Nat. Rev. Microbiol.* **19**, 319–330 (2021).
45. Goyal, S., Yuan, J., Chen, T., Rabinowitz, J. D. & Wingreen, N. S. Achieving optimal growth through product feedback inhibition in metabolism. *PLoS Comput. Biol.* **6**, e1000802 (2010).
46. Weimar, J. D., DiRusso, C. C., Delio, R. & Black, P. N. Functional role of fatty acyl-coenzyme A synthetase in the transmembrane movement and activation of exogenous long-chain fatty acids. Amino acid residues within the ATP/AMP signature motif of Escherichia coli FadD are required for enzyme activity and fatty acid transport. *J. Biol. Chem.* **277**, 29369–29376 (2002).
47. May, K. L. & Silhavy, T. J. The *Escherichia coli* phospholipase PldA regulates outer membrane homeostasis via lipid signaling. *mBio* **9**, e00379–18 (2018).
48. Zhang, Y.-M. & Rock, C. O. Membrane lipid homeostasis in bacteria. *Nat. Rev. Microbiol.* **6**, 222–233 (2008).
49. Tsay, J. T., Oh, W., Larson, T. J., Jackowski, S. & Rock, C. O. Isolation and characterization of the beta-ketoacyl-acyl carrier protein synthase III gene (fabH) from *Escherichia coli* K-12. *J. Biol. Chem.* **267**, 6807–6814 (1992).
50. Yao, Z., Davis, R. M., Kishony, R., Kahne, D. & Ruiz, N. Regulation of cell size in response to nutrient availability by fatty acid biosynthesis in *Escherichia coli*. *Proc. Natl Acad. Sci. USA*. **109**, E2561–E2568 (2012).
51. Wong, F. et al. Cytoplasmic condensation induced by membrane damage is associated with antibiotic lethality. *Nat. Commun.* **12**, 2321 (2021).
52. Kohanski, M. A., Dwyer, D. J., Hayete, B., Lawrence, C. A. & Collins, J. J. A common mechanism of cellular death induced by bactericidal antibiotics. *Cell* **130**, 797–810 (2007).
53. Zhao, Y. et al. SoNar, a highly responsive NAD+/NADH sensor, allows high-throughput metabolic screening of anti-tumor agents. *Cell Metab.* **21**, 777–789 (2015).
54. Kohanski, M. A., Dwyer, D. J., Wierzbowski, J., Cottarel, G. & Collins, J. J. Mistranslation of membrane proteins and two-component system activation trigger antibiotic-mediated cell death. *Cell* **135**, 679–690 (2008).
55. Shi, H. et al. Starvation induces shrinkage of the bacterial cytoplasm. *Proc. Natl Acad. Sci. USA* **118**, e2104686118 (2021).
56. Haxim, Y. et al. Autophagy functions as an antiviral mechanism against geminiviruses in plants. *eLife* **6**, e23897 (2017).
57. Xu, J.-Y. et al. Integrative proteomic characterization of human lung adenocarcinoma. *Cell* **182**, 245–261.e17 (2020).
58. Cappelletti, V. et al. Dynamic 3D proteomes reveal protein functional alterations at high resolution in situ. *Cell* **184**, 545–559.e22 (2021).
59. Piazza, I. et al. A map of protein-metabolite interactions reveals principles of chemical communication. *Cell* **172**, 358–372.e23 (2018).
60. Schmidt, A. et al. The quantitative and condition-dependent Escherichia coli proteome. *Nat. Biotechnol.* **34**, 104–110 (2016).
61. Tatusov, R. L. et al. The COG database: an updated version includes eukaryotes. *BMC Bioinform.* **4**, 41 (2003).
62. Galperin, M. Y., Makarova, K. S., Wolf, Y. I. & Koonin, E. V. Expanded microbial genome coverage and improved protein family annotation in the COG database. *Nucleic Acids Res.* **43**, D261–D269 (2015).
63. Reichl, B. et al. Evaluation and optimization of common lipid extraction methods in cerebrospinal fluid samples. *J. Chromatogr. B* **1153**, 122271 (2020).
64. Lennen, R. M. & Pfleger, B. F. Modulating membrane composition alters free fatty acid tolerance in *Escherichia coli*. *PLoS ONE* **8**, e54031 (2013).
65. Guo, W., Sheng, J. & Feng, X. 13C-Metabolic flux analysis: an accurate approach to demystify microbial metabolism for biochemical production. *Bioengineering* **3**, 3 (2015).
66. Antoniewicz, M. R. 13C metabolic flux analysis: optimal design of isotopic labeling experiments. *Curr. Opin. Biotechnol.* **24**, 1116–1121 (2013).
67. Liu, J. et al. Metabolic co-dependence gives rise to collective oscillations within biofilms. *Nature* **523**, 550–554 (2015).

Acknowledgements

We thank Fan Bai in Peking University for kindly providing bacterial strains (membrane potential sensor ViBac2). This work was supported by the National Nature Science Foundation of China (32470049) and Tianjin

Synthetic Biotechnology Innovation Capacity Improvement Project, China (TSBICIP-CXRC-078).

Author contributions

Y.Z., Y.C., and Y.-H.P.J.Z. designed the study, Y.Z. designed the microfluidic chip, Y.Z. and Y.C. performed the experiments, Y.Z., Y.C., and B.Z. analyzed the data, Y.Z., B.Z., and Y.-H.P.J.Z. wrote and revised the manuscript, all authors discussed the manuscript.

Competing interests

The authors declare no competing interests.

Additional information

Supplementary information The online version contains supplementary material available at https://doi.org/10.1038/s41467-024-51940-3.

Correspondence and requests for materials should be addressed to Yuzhen Zhang or Yi-Heng P. Job Zhang.

Peer review information *Nature Communications* thanks Romain Briandet and Sammy Pontrelli for their contribution to the peer review of this work. A peer review file is available.